CARBON 80 (2014) 246–254

Available at www.sciencedirect.com

ScienceDirect

journal homepage: www.elsevier.com/locate/carbon

High-performance supercapacitors based on defect-engineered carbon nanotubes

Young Soo Yun [a,b], Gabin Yoon [b,c], Kisuk Kang [b,c], Hyoung-Joon Jin [a,*]

[a] Department of Polymer Science and Engineering, Inha University, Incheon 402-751, Republic of Korea

[b] Department of Materials Science and Engineering, Research Institute of Advanced Materials (RIAM), Seoul National University, Gwanak-ro 599, Gwanak-gu, Seoul 151-742, Republic of Korea

[c] Center for Nanoparticle Research, Institute for Basic Science (IBS), Seoul National University, Gwanak-ro 599, Gwanak-gu, Seoul 151-742, Republic of Korea

ARTICLE INFO

Article history:
Received 25 February 2014
Accepted 18 August 2014
Available online 23 August 2014

ABSTRACT

Defect-engineered carbon nanotubes (CNTs) were prepared by KOH activation and subsequent nitrogen doping. Controlled KOH activation of the CNTs enlarged the specific surface area to 988 $m^2 g^{-1}$, which is about 4.5 times greater than that of pristine CNTs. In addition, a hierarchical pore structure and a rough surface developed at high degrees of activation, which are advantageous features for fast ion diffusion. The subsequent nitrogen doping changed the band structure of the CNTs, resulting in improved electrical properties. Symmetric supercapacitors fabricated using these nitrogen-doped and activated CNTs (NA-CNTs) successfully worked across a wide potential range (0–3.5 V) and exhibited a high capacitance of 98 F g^{-1} at a current density of 1 A g^{-1}. Furthermore, a low equivalent series resistance (2.2 Ω) was achieved owing to the tailored nanostructure and electrical properties of the electrode materials. Over the voltage range from 0 to 3.5 V, supercapacitors based on NA-CNTs exhibited a high specific energy of 59 Wh kg^{-1} and a specific power of 1750 W kg^{-1}. In addition, a specific power of 52,500 W kg^{-1} with a 3-s charge/discharge rate was achieved with a specific energy of 26 Wh kg^{-1}. Moreover, the supercapacitors showed stable performance over 10,000 charge/discharge cycles.

1. Introduction

Supercapacitors have recently received much attention for their potential as energy-storage devices owing to their high rate capability, good reversibility, and long cycle life [1–3]. However, their low energy density (about 5 Wh kg^{-1}) compared to conventional batteries limits their suitability for applications in electric vehicles, portable power tools, and uninterruptible power supplies [1–3]. Furthermore, the power levels of current commercial supercapacitors are not sufficient to meet emerging needs [4]. The energy density (E) of a supercapacitor is related to its cell voltage (V) and capacitance (C) according to $E = 1/2CV^2$ [5,6], whereas the maximum power density (P) is given by $P_{max} = V_i^2/4R$, where R is the equivalent series resistance (ESR) [5,6]. These equations show that, to obtain high-performance supercapacitors, a high working voltage and a low ESR are essential.

Nanohybrid materials, such as metal oxides or conducting polymers combined with carbon, have been studied by various groups with the aim of achieving enhanced energy densities in supercapacitors [7–11]. Such nanohybrids often exhibit high capacitance, but pseudo-capacitive electrodes based on

* *Corresponding author:* Fax: +82 32 865 5178.
E-mail address: hjjin@inha.ac.kr (H.-J. Jin).

http://dx.doi.org/10.1016/j.carbon.2014.08.063
0008-6223/

them are limited by the properties of the aqueous electrolyte to a voltage of around 1 V. To overcome this limitation, asymmetric supercapacitors have been developed that are capable of operating across a wide range of voltages, well above those of aqueous-electrolyte-based devices [12–14]. These asymmetric supercapacitors also exhibit high capacitances and high specific energies, but their power characteristics and cycle stabilities are still insufficient for practical applications. Recently, it was demonstrated that carbon-based electrode materials could be used across a wide range of potentials in an ionic liquid electrolyte [15]. This suggests that high-performance supercapacitors could be achieved through a sophisticated electrode design, employing well-defined and tailored carbon nanomaterials.

Carbon nanotubes (CNTs) are particularly promising as supercapacitor electrode materials as a result of their superior electrical properties and well-defined nanostructures [16–19]. However, CNTs provide smaller surface area and micropore content than conventional activated carbon (AC), which has so far resulted in insufficient capacitance in CNT-based electrodes. Consequently, the preparation of defective CNTs by KOH activation has been suggested as a way to enhance their surface area through the formation of defects, such as cavities and open ends [20,21]. However, further studies into this concept are required to ensure the effective design of supercapacitor electrodes incorporating such defective materials. Additionally, the doping of a CNT surface by foreign atoms can also improve its physical properties. For example, doping with nitrogen modifies the conduction band and leads to a larger electron donor state [22,23]. Such modification of the electronic structure has the potential to enhance the electrical conductivity and quantum capacitance of CNTs [24,25], and thus, nitrogen-doped CNTs may contribute in their own way to improving the power characteristics of supercapacitors [26].

In this study, defect-engineered CNTs were prepared by controlled KOH activation and subsequent nitrogen doping with melamine. The porosity of the CNTs was tailored by this activation scheme, resulting in a high surface area and hierarchical pore-size distribution. This, in turn, increased the specific capacitance and improved the rate performance by facilitating fast ion diffusion. Furthermore, nitrogen doping of the activated CNT (A-CNT) surface contributed to the rate performance increase by enhancing its electrical properties. Supercapacitors fabricated using these nitrogen-doped activated CNTs (NA-CNTs) possessed high specific capacities and good power characteristics. In addition, good cycle stability was achieved.

2. Experimental

2.1. Preparation of A-CNTs and NA-CNTs

Various quantities of KOH (5, 13, 25, 37.5, 50, 62.5, and 75 g) were added to 5 g samples of pristine CNTs (P-CNTs, CM-95, Hanhwa Chemical Co., Ltd., Seoul, Korea). These mixtures were then activated by heating them to 800 °C for 2 h at a heating rate of 10 °C min^{-1} under Ar flowing at 200 mL min^{-1}. The resulting A-CNTs were washed using distilled water and ethanol (99.9%, OCI Company, Atlanta, GA, USA) and then dried in a vacuum oven at 30 °C. Nitrogen doping of the A-CNTs was performed using an aqueous solution containing melamine as follows. First, 100 mg of melamine was dissolved in 100 g of distilled water at 60 °C. Next, 100 mg of A-CNTs were dispersed in this solution by sonication, and the resulting solution was then frozen in liquid nitrogen and freeze-dried using a lyophilizer at −50 °C and 0.0045 mbar for 72 h. Following lyophilization, the mixture was thermally treated in a tubular furnace by heating to 600 °C at a rate of 10 °C min^{-1} under Ar flowing at 200 mL min^{-1}. This reaction mixture was then held at 600 °C for 2 h, and the resulting NA-CNT products were transferred to a vacuum oven for storage at 30 °C.

2.2. Characterization

The morphology of the prepared samples was examined using field-emission scanning electron microscopy (FE-SEM, S-4300, Hitachi, Tokyo, Japan) and field-emission transmission electron microscopy (FE-TEM, JEM2100F, JEOL, Tokyo, Japan). The chemical composition of the samples was evaluated using X-ray photoelectron spectroscopy (XPS, PHI 5700 ESCA, Chanhassen, MN, USA) with monochromatic Al Kα radiation ($h\nu$ = 1486.6 eV) and elemental analysis with an EA1112 (CE instrument, Italy). In addition, the Brunauer–Emmett–Teller (BET) specific surface area and average pore diameter were determined from nitrogen adsorption/desorption isotherms (ASAP 2020, Micromeritics, Norcross, GA, USA) at −196 °C. Raman spectra were recorded using a continuous-wave linearly polarized laser with a wavelength of 473 nm (2.62 eV), 50-μm pinhole, and 600-groove/mm grating. To ensure nondestructive measurements, a low laser power of <300 μW was used to irradiate the samples.

2.3. Electrochemical characterization

Electrochemical measurements were performed using a two-electrode system. The NA-CNTs, A-CNTs, P-CNTs, and AC (Kansai Netsukagaku Co., Hyogo, Japan) were first mixed individually into a paste containing 5 wt.% poly-vinylidenefluoride (Sigma–Aldrich, St. Louis, MO, USA). Electrodes, which were 1 cm in diameter and approximately 100 μm thick, were formed from the thick slurry and pressed onto aluminum current collectors. A typical pair of electrodes weighed between 5 and 6 mg after drying overnight at 100 °C. A mixture of 1-butyl-3-methylimidazolium tetrafluoroborate (BMIM BF_4) and acetonitrile (AN) in a weight ratio of 1:1 was used as the electrolyte. The electrodes and a porous polypropylene separator (Whatman GF/D, Piscataway, NJ, USA) were sandwiched together in a stainless steel cell to form the two-electrode cell device. All cell preparation steps were conducted in an Ar-filled glove box; the oxygen and water levels were each maintained below 1 ppm.

Electrochemical performance data was obtained by cyclic voltammetry, chronopotentiometry, and electrical impedance spectroscopy (EIS) (PGSTAT302N, Metrohm Autolab, Utrecht, The Netherlands) measurements. The specific capacitance of the supercapacitors was determined from the galvanostatic measurements using

$$C = \frac{4I_{cons}}{m dV/dt}, \quad (1)$$

where I_{cons} is the (constant) current, m is the total mass of both carbon electrodes, and dV/dt was calculated from the slope of the discharge curve over the range from $V = V_{max}$ (the voltage at the beginning of discharge) to $V = 1/2V_{max}$. The specific power density and energy density of the supercapacitors were also calculated as follows:

$$P = \Delta V \times I/m, \quad (2)$$

$$E = P \times t/3600, \quad (3)$$

and

$$\Delta V = (E_{max} + E_{min})/2 \quad (4)$$

In Eqs. (2)–(4), E_{max} and E_{min} are the potentials at the beginning and the end of discharge (in V), respectively, I is the charge/discharge current (in A), t is the discharge time (in s), and m is the total mass (in kg) of active materials, including both electrodes, in the symmetric supercapacitors. A current density ranging from 1 to 30 A g^{-1} was applied to all of the cells, while the potential between the two electrodes was swept between the cutoff values of 0 and 3.5 V. For the cycling test, a current density of 3 A g^{-1} was applied.

2.4. *First-principles simulation*

All first-principles calculations were performed using the local density approximation (LDA) and the Perdew–Burke–Ernzerhof (PBE) function for the exchange-correlation parametrization [27]. A plane-wave basis set and the projector-augmented wave (PAW) method were also used, as implemented in the Vienna *ab initio* simulation package (VASP) code [28]. We employed a semiconducting (8, 0) carbon nanotube with a diameter of 6.26 Å and a length of 8.52 Å as a model system to calculate the density of states (DOS) profiles for the P-CNTs and NA-CNTs. Because periodic boundary conditions are applied in VASP, 10 Å vacuum slabs were employed in all directions to prevent any interaction between the CNTs. We also used k-points from $4 \times 4 \times 8$ Gamma-centered grids and a kinetic energy cutoff of 400 eV in all calculations.

3. Results and discussion

The morphologies of the A-CNTs and NA-CNTs were found to be quite similar, as shown in the FE-TEM images in Fig. 1. Some wall regions of the defective CNTs were fully damaged and peeled, and numerous nanocavities developed on the CNT surfaces. These nanocavities developed during the activation of the carbon with KOH, which proceeds according to the reaction $K_2O + C \rightarrow 2\,K + CO$ at temperatures higher than 700 °C [29,30]. The resulting K intercalated into the CNTs, and intrinsic defect sites were attacked preferentially. Several different types of CNTs were identified based on the bending ratio (Fig. S1), as this ratio is closely related to the number of intrinsic defects [31]. Those CNTs with a high bending ratio tended to be more strongly activated than the others. In contrast, single-walled CNTs (SWCNTs), which have very low levels of intrinsic defects compared with multiwalled CNTs, were hardly activated under the same conditions (Fig. S2).

The results of the activation process also depended on the ratio of KOH to P-CNTs, so various ratios from 1:1 to 15:1 were tested to obtain A-CNTs with a range of surface areas. In this study, a KOH:P-CNT ratio of 7.5:1 produced the highest surface areas of all investigated ratios. (The specific surface areas of the samples are shown in Fig. S3.) The NA-CNTs with high bending ratios contained a large volume of nanocavities and had a high surface area following KOH activation (KOH:P-CNT ratio of 7.5) and nitrogen doping (Fig. 2). The nitrogen adsorption and desorption isotherms of the NA-CNTs shown in Fig. 2(a) show hybrid IUPAC Type-I and Type-IV shapes, indicating the existence of domains with microporous and mesoporous structures. In contrast, the isothermal curves of the P-CNTs matched a pure IUPAC Type-IV shape, indicating a mesoporous structure. This difference in structure is further confirmed by their respective pore-size distributions, as shown in Fig. 2(b). The NA-CNTs show a greater number of pores of all sizes than the P-CNTs, with the occurrence of 2–3 nm pores, in particular, being notably more frequent in the NA-CNTs. The peeled walls and open ends produced during KOH activation can potentially enlarge the volume of mesopores, thus creating more efficient pathways for ion diffusion. Furthermore, the large number of nanopores induced by nanocavities on the surface of the NA-CNTs enhance charge storage. The specific surface area of the NA-CNTs was found to be 988 $m^2\,g^{-1}$, which is 4.5 times higher than that of the P-CNTs (217 $m^2\,g^{-1}$). The bulk density of the NA-CNTs, calculated using the Barrett–Joyner–Halender (BJH) method, is 0.58, and the packing densities are ~0.49. The packing density was calculated by filling a calibrated cylinder with a known sample

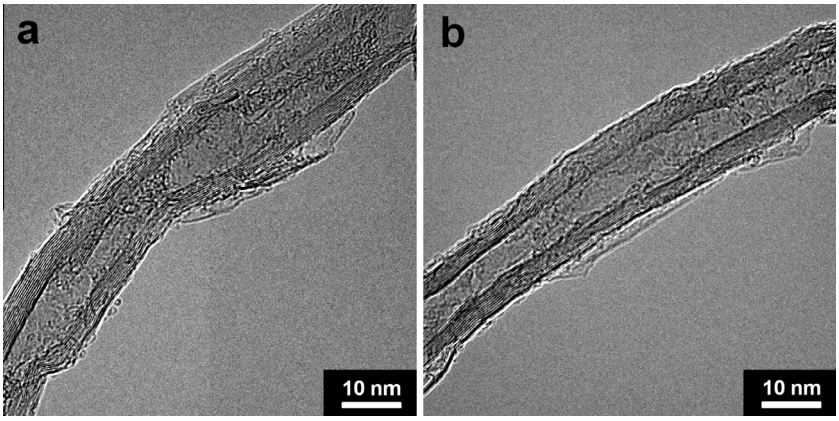

Fig. 1 – Representative FE-TEM images of (a) A-CNT and (b) NA-CNT.

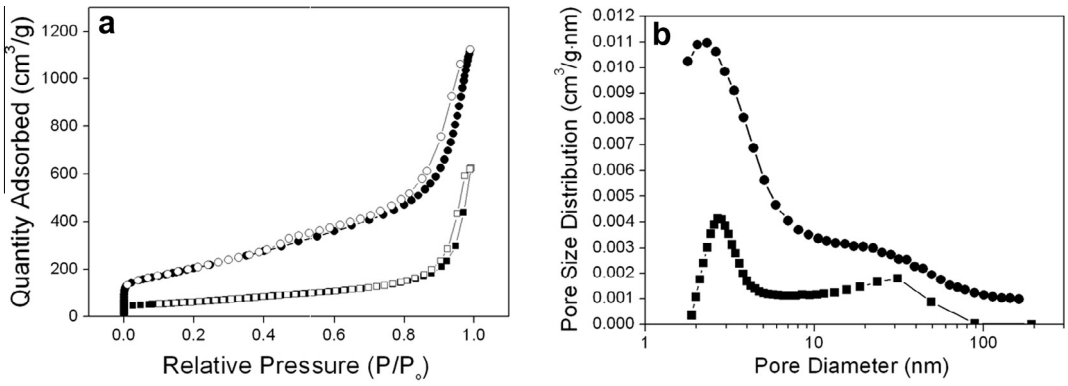

Fig. 2 – (a) Nitrogen adsorption and desorption isotherms of P-CNTs (squares) and NA-CNTs (circles), and (b) pore-size distributions in P-CNTs (squares) and NA-CNTs (circles).

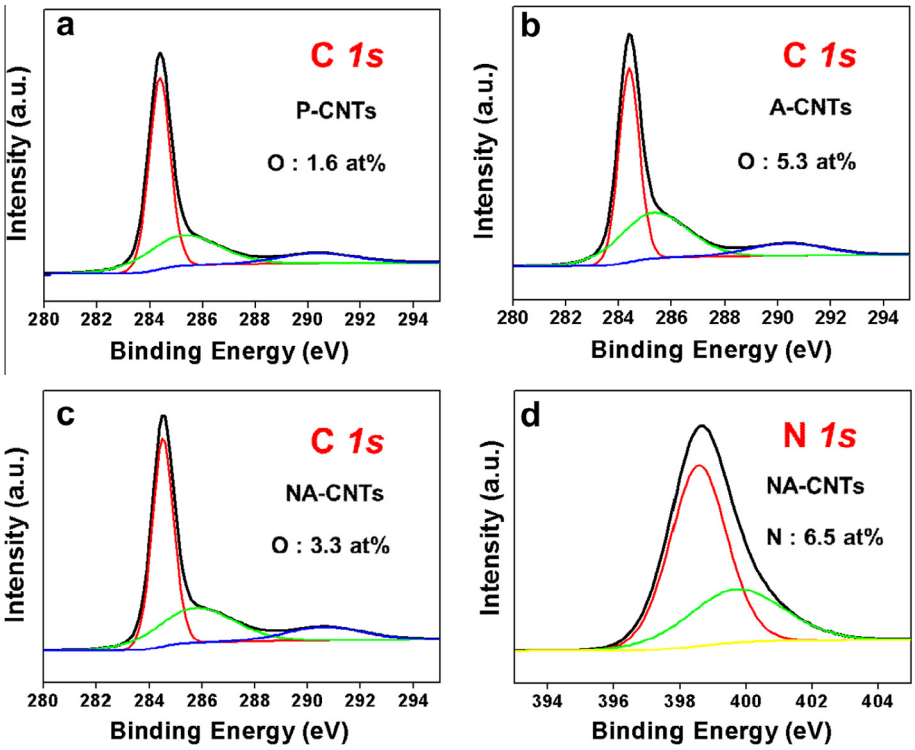

Fig. 3 – XPS C 1s spectra of (a) P-CNTs, (b) A-CNTs, and (c) NA-CNTs, and (d) XPS N 1s spectra of NA-CNTs. (A color version of this figure can be viewed online.)

weight and tapping the cylinder until a minimum volume was recorded. These calculated densities were similar to those of typical ACs (0.45–0.55 g cm^{-3}).

The chemical-bonding environment in the P-CNTs also changed as a result of KOH activation. In particular, the XPS C 1s spectrum of the P-CNTs shown in Fig. 3(a) exhibits distinct peaks, such as an sp^3 C–C and C–O peak centered at 285.5 eV and a C(O)–O peak centered at 290.3 eV, including a main sp^2 C=C peak at 284.6 eV. Similar peaks were also observed in the XPS C 1s spectra of the A-CNTs (Fig. 3(b)); however, the intensity of the peak centered at 285.6 eV and the oxygen content (5.3 at.%) were higher. These results confirmed that a multitude of defects and oxygen functional groups were introduced to the surface of the CNTs after KOH activation. Subsequent thermal treatment with melamine further affected the chemical-bonding environment in the A-CNTs, with the XPS C 1s spectrum of the NA-CNTs shown in Fig. 3(c) exhibiting peaks similar to those of the P-CNTs and A-CNTs. However, the peak centered at 285.6 eV for the A-CNTs was shifted to 285.9 eV, became less intense, and broadened. Furthermore, the oxygen content of the A-CNTs was reduced to 3.3 at.% in the NA-CNTs; this could be attributed to the newly formed C–N bonds and an associated reduction in the prevalence of the sp^3 C–C configuration.

The XPS N 1s spectrum of the NA-CNTs shown in Fig. 3(d) shows two distinct peaks, centered at 398.5 eV and 399.8 eV, indicating six-membered (pyridinic N) and five-membered

(pyrrolic N) rings, respectively, at the edges of the graphene sheets. The surface nitrogen content of the NA-CNTs calculated by XPS was 6.5 at.%, which is comparable to about 7.4 wt.%. In contrast, the results of the elemental analysis show that NA-CNTs have a total nitrogen content of 4.8 wt.%. These results demonstrate that the nitrogen groups have been mainly introduced on the surface of the A-CNTs. The presumed nitrogen doping process by melamine molecules occurs as follows: (1) melamine molecules are absorbed on the surface of A-CNTs *via* π–π interactions and hydrogen bonding with oxygen functional groups; (2) during the thermal treatment, the nitrogen functional groups of melamine molecules react with oxygen functional groups or defect sites of A-CNTs and/or are condensed to carbon nitride on the surface of A-CNTs; [32] and (3) the doped nitrogen compounds are transformed to thermo-stable aromatic structures such as pyridinic or pyrrolic rings on the surface of A-CNTs.

Fig. 4(a) shows the XRD patterns obtained from the P-CNTs, A-CNTs, and NA-CNTs. Two peaks were observed at 25.8° and 42.8°, which correspond to the degree of stacking ordering of the layered carbon structure (002) and ordered hexagonal carbon structure (100), respectively. The (002) peak for the A-CNTs was broader than that of the P-CNTs. This could be interpreted as damage to and/or a decrease in the size of the layered carbon structure. Furthermore, the (002) peak of the NA-CNTs had a 2θ value of 26.0° but a broader peak width than that of the P-CNTs. These results mean that the defective graphitic layers in the A-CNTs recovered, and the peak broadening in the NA-CNTs pattern could be induced by a decrease in the size of the graphitic layers during activation. In contrast, the (100) peak of the NA-CNTs was significantly narrower than that of the P-CNTs, indicating that a more ordered hexagonal structure was developed.

Further study of the crystal structure was performed by the collection of Raman spectra. Fig. 4(b) shows the Raman spectra of the P-CNTs, A-CNTs, and NA-CNTs, in which the usual *D* and *G* band peaks for CNTs are present. The *D* band characterizes the disorder in the CNTs, whereas the *G* band is assigned to the hexagonal carbon structure. The Raman spectra of all samples show intense *D* bands localized at ~1326 cm^{-1}, which are assigned to disorder originating from sp^3 carbons. The *G* bands, which reflect the graphite-like structure of the CNTs, are split into two components. The G^- mode is typically assigned to the plasma resonance associated with atomic displacement along the circumference of the CNTs [33], while the G^+ band is associated with defect structures [34] and displacements of carbon atoms along the axis of the nanotubes. For semiconducting nanotubes, both G^- and G^+ have similar widths; whereas for metallic tubes, the intensity of the G^- mode is higher, and the peak shifts to a lower energy and becomes broader and more symmetric [35].

In the P-CNTs, the relative intensity of the *G* band to the *D* band was increased by KOH activation. In the course of the activation process, the intrinsic defect sites in the P-CNTs were preferentially attacked and removed, while thermal treatment with melamine induced more ordered hexagonal carbon structures. Consequently, the hexagonal carbon structure was more strongly expressed in the NA-CNTs than in the P-CNTs. Furthermore, the intensity of the G^- (~1576 cm^{-1}) mode was much higher for the NA-CNTs than for the P-CNTs (~1579 cm^{-1}), and the peak was shifted to a lower energy. This means that the NA-CNTs are more metallic in nature than the P-CNTs.

This result is further supported by the first-principles calculations. Fig. 5 shows the modeled structures and DOS profiles of the P-CNTs and the NA-CNTs. Note that the DOS profile of (8, 0) P-CNT exhibited a bandgap of ~0.5 eV, indicating that this material has semiconducting characteristics. However, energy states at the Fermi energy level were observed in the case of NA-CNTs, indicating that no band gap is present and that the material has metallic properties. Pyridine-like dopant nitrogen atoms in the CNTs create donor states around the Fermi level, and the interactions among these nitrogen dopants result in a broadening of the energy ranges of the donor states. This in turn leads to band formation, and thus, the CNTs are metallic because of the nitrogen dopants. Moreover, additional charge carriers are introduced upon nitrogen doping. It is expected that NA-CNTs will exhibit a higher electronic conductivity than P-CNTs, which should enhance the rate capability of NA-CNT-based supercapacitors.

The electrochemical performance of the NA-CNT-based supercapacitors was analyzed using an organic electrolyte: BMIM BF_4/AN. The cyclic voltammograms of the NA-CNT-based supercapacitors shown in Fig. 6(a) all exhibit

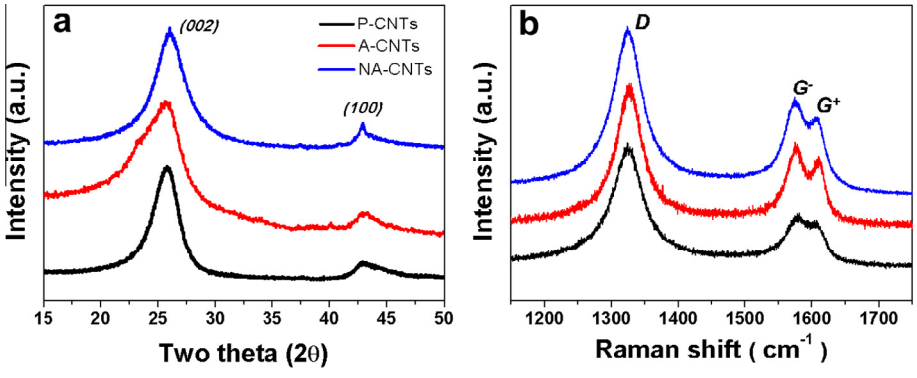

Fig. 4 – (a) XRD patterns and (b) Raman spectra of P-CNTs (black), A-CNTs (red), and NA-CNTs (blue). (A color version of this figure can be viewed online.)

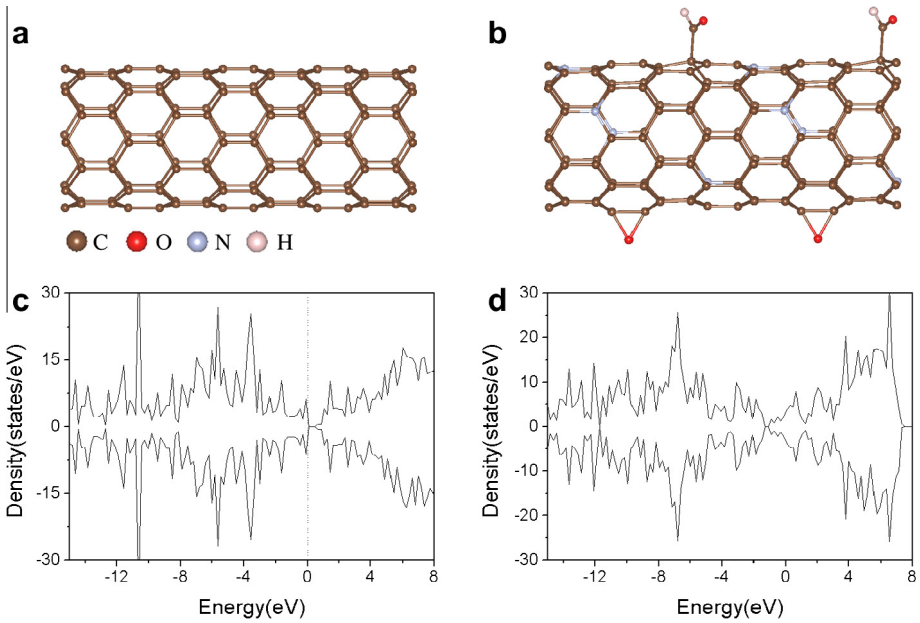

Fig. 5 – Modeled structures of (a) a P-CNT and (b) a NA-CNT, and DOS profiles of (c) P-CNTs and (d) NA-CNTs. The NA-CNTs contain 6.25 at.% pyridine-like N atoms and 3.13 at.% O atoms present in both C–O and C═O bonds. (A color version of this figure can be viewed online.)

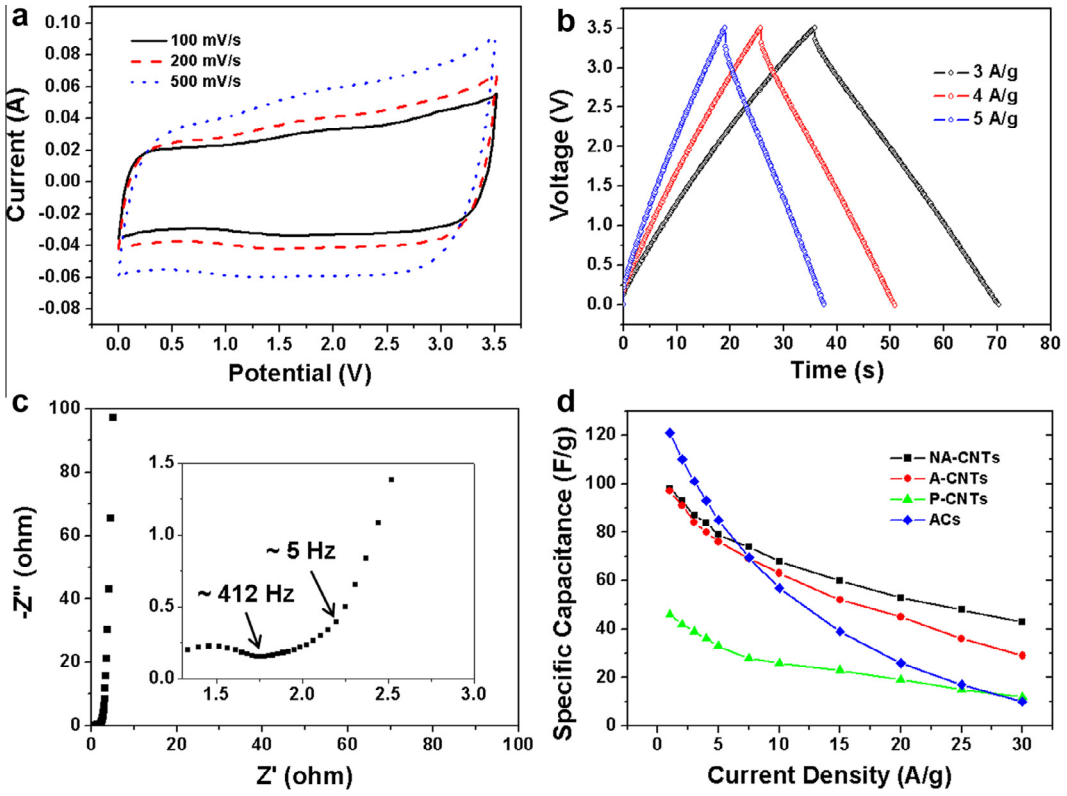

Fig. 6 – (a) Cyclic voltammograms of NA-CNT-based supercapacitors obtained at scan rates of 100 (black, solid line), 200 (red, dashed line), and 500 mV/s (blue, dotted line). (b) Galvanostatic charge/discharge curves of NA-CNTs at current densities of 3 (black), 4 (red), and 5 A g^{-1} (blue) over a potential range from 0 to 3.5 V in BMIM BF_4/AN electrolyte. (c) Nyquist plot of NA-CNTs in the frequency range from 100 kHz to 0.1 Hz. (d) Specific capacitances of the ACs, P-CNTs, A-CNTs, NA-CNTs measured at various current densities over a potential range from 0 to 3.5 V in BMIM BF_4/AN electrolyte. (A color version of this figure can be viewed online.)

rectangular shapes, indicating ideal capacitive behavior over a wide electrochemical voltage range. The steep slopes of the current change at the switching potentials indicate a small mass-transfer resistance. The porous structure of the NA-CNTs facilitated this ideal capacitive behavior by allowing fast ionic motion, and these capacitive behaviors were maintained at a scan rate of 500 mV s^{-1}. In addition, the galvanostatic charge/discharge curves of the NA-CNT-based supercapacitors at current densities of 3, 4, and 5 A g^{-1} shown in Fig. 6(b) exhibited lower dynamic voltage (IR) drops in spite of their higher electrochemical potential of 3.5 V.

These high-power characteristics are further illustrated by the Nyquist plot of the NA-CNT-based supercapacitors in the frequency range from 100 kHz to 0.1 Hz in Fig. 6(c). This plot features a vertical line in the low-frequency region, which represents ideal capacitive behavior. From the magnified data in the high-frequency range, a transition between the RC semicircle and the migration of the electrolyte was observed at a frequency of about 412 Hz. This corresponds to a resistance of 1.8 Ω, which is much smaller than that of activated-graphene-based supercapacitors [15]. The diffusion of electrolyte ions stopped at about 5 Hz, below which capacitive behavior is observed. The ESR of the NA-CNT-based supercapacitors is about 2.2 Ω, which indicates that these materials have a low internal resistance because of the easy accessibility of the pores to the electrolyte ions and the high electrical conductivity.

The specific capacitance of the NA-CNT-based supercapacitors was determined to be 98 F g^{-1} at a current density of 1 A g^{-1} (Fig. 6(d)). This value corresponds to the volumetric capacitance of 48 F cc^{-1}, which is lower than the 121 F g^{-1} of the AC-based supercapacitors and similar to the 97 F g^{-1} of the A-CNT-based. However, with an increase in the current density, the decrease in capacitance is more pronounced for AC- and A-CNT-based supercapacitors than for NA-CNT-based supercapacitors, a phenomenon that is closely related to the voltage (IR) loss of the samples. Because NA-CNTs have a well-developed porous nanostructure and good electrical conductivity, they exhibit fast ion diffusion and electron conduction. Consequently, at a high current density of 30 A g^{-1}, the NA-CNT-based supercapacitors maintained a capacitance of 42 F g^{-1}, which is approximately three times higher than that of the AC- and P-CNT-based supercapacitors.

Furthermore, the energy density reached a maximum of 59 Wh kg^{-1} at a power density of 1750 W kg^{-1}, as shown in Fig. 7. This value is significantly higher than that of the asymmetric hybrid supercapacitors based on CNTs, including TiO_2 nanowires/CNTs [36], CNTs/V_2O_5-AC [37], and $Ni(OH)_2$/CNTs-AC materials [13]. The power density is similar to that of SWCNT-based symmetric supercapacitors [38], but an energy density four times greater was achieved. Even at a 3-s charge/discharge rate (at a power density of 52,500 W kg^{-1}), an energy density as high as 26 Wh kg^{-1} was retained. The packaged supercapacitor devices contain active electrode materials of ~30 wt.% [15]. Therefore, the NA-CNT-based supercapacitors have a practical energy density of ~18 Wh kg^{-1}. This energy density is three times higher than existing AC-based supercapacitors. In addition, this superior performance can be maintained up to 10,000 charge/discharge cycles; Fig. 8 shows that capacitance retention of 91% was achieved.

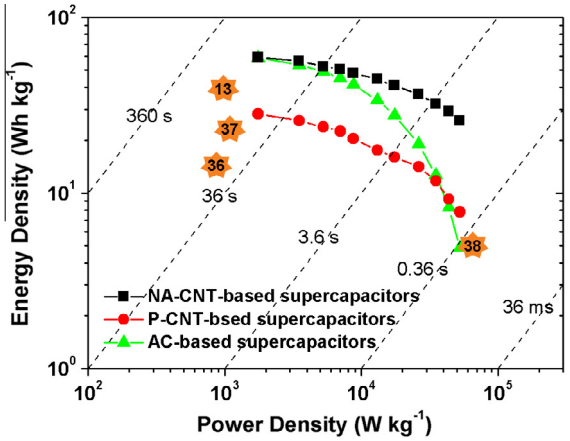

Fig. 7 – Ragone plot of NA-CNT – (■), P-CNT-based (●) and AC-based (▲) supercapacitors, including reference values for TiO_2 nanowires/CNT – [36], CNT/V_2O_5-AC – [37], $Ni(OH)_2$/CNT-AC – [13], and SWCNT-based devices [38]. (A color version of this figure can be viewed online.)

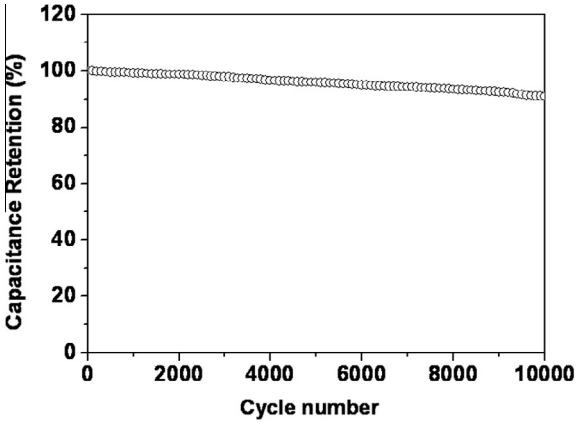

Fig. 8 – Capacitance retention of supercapacitors based on NA-CNTs during 10,000 charge/discharge cycles at a current density of 3 A g^{-1}.

4. Conclusion

Carbon nanotubes (CNTs) with different bending ratios were activated by KOH at various KOH:CNT weight ratios. The CNTs with a high bending ratio were more strongly activated, and activated CNTs produced at a KOH:CNT ratio of 7.5 were found to have a hierarchical pore structure and the highest surface area of all samples tested. Following nitrogen doping, the semiconducting electronic structure of the activated CNTs changed to a metallic electronic structure. These doped, activated CNTs retained a high surface area of 988 m^2 g^{-1} with a nitrogen fraction of 6.5 at.% and exhibited a high specific capacitance of 98 F g^{-1} at a current density of 1 A g^{-1} over a voltage range of 0–3.5 V. At a high current density of 30 A g^{-1}, the NA-CNT-based supercapacitors maintained a capacitance of 42 F g^{-1}, which is approximately three times

higher than that of activated-carbon- and pristine-CNT-based supercapacitors. The energy and power densities of the doped, activated CNT-based supercapacitors reached 59 Wh kg^{-1} and 52,500 W kg^{-1}, respectively, and possessed a stable lifetime over 10,000 cycles.

Acknowledgments

This work was supported by a National Research Foundation of Korea Grant (NRF-2010-C1AAA001-0029018), funded by the Korean Government (MEST) and by Basic Science Research Program through the NRF funded by the Ministry of Education (NRF-2013R1A1A2A10008534).

Appendix A. Supplementary data

Supplementary data associated with this article can be found, in the online version, at http://dx.doi.org/10.1016/j.carbon.2014.08.063.

REFERENCES

[1] Simon P, Gogotsi Y. Materials for electrochemical capacitors. Nat Mater 2008;7(11):845–54.
[2] Miller JR, Simon P. Electrochemical capacitors for energy management. Science 2008;321(5889):651–2.
[3] Aricò AS, Bruce P, Scrosati B, Tarascon J-M, Schalkwijk WV. Nanostructured materials for advanced energy conversion and storage devices. Nat Mater 2005;4(5):366–77.
[4] Burke A. Ultracapacitors: why, how, and where is the technology. J Power Sources 2000;91(1):37–50.
[5] Yun YS, Cho SY, Shim J, Kim BH, Chang S-J, Baek SJ, et al. Microporous carbon nanoplates from regenerated silk proteins for supercapacitors. Adv Mater 2013;25(14):1993–8.
[6] Yun YS, Im C, Park HH, Hwang I, Tak Y, Jin H-J. Hierarchically porous carbon nanofibers containing numerous heteroatoms for supercapacitors. J Power Sources 2013;234(1):285–91.
[7] Lee SW, Kim J, Chen S, Hammond PT, Shao-Horn Y. Carbon nanotube/manganese oxide ultrathin film electrodes for electrochemical capacitors. ACS Nano 2010;4(7):3889–96.
[8] Liu J, Essner J, Li J. Hybrid supercapacitor based on coaxially coated manganese oxide on vertically aligned carbon nanofiber arrays. Chem Mater 2010;22(17):5022–30.
[9] Biswas S, Drzal LT. Multilayered nanoarchitecture of graphene nanosheets and polypyrrole nanowires for high performance supercapacitor electrodes. Chem Mater 2010;22(20):5667–71.
[10] Chen S, Zhu J, Wu X, Han Q, Wang X. Graphene oxide–MnO_2 nanocomposites for supercapacitors. ACS Nano 2010;4(5):2822–30.
[11] Im C, Yun YS, Kim B, Park HH, Jin H-J. Amorphous carbon nanotube/MnO_2/graphene oxide ternary composite electrodes for electrochemical capacitors. J Nanosci Nanotechnol 2013;13(3):1765–8.
[12] Chen P-C, Shen G, Shi Y, Chen H, Zhou C. Preparation and characterization of flexible asymmetric supercapacitors based on transition-metal-oxide nanowire/single-walled carbon nanotube hybrid thin-film electrodes. ACS Nano 2010;4(8):4403–11.
[13] Tang Z, Tang CH, Gong H. A high energy density asymmetric supercapacitor from nano-architectured $Ni(OH)_2$/carbon nanotube electrodes. Adv Funct Mater 2012;22(6):1272–8.
[14] Chen Z, Augustyn V, Wen J, Zhang Y, Shen M, Dunn B, et al. High-performance supercapacitors based on intertwinded CNT/V_2O_5 nanowire nanocomposites. Adv Mater 2011;23(6):791–5.
[15] Zhu Y, Murali S, Stoller MD, Ganesh KJ, Cai W, Ferreira PJ, et al. Carbon-based supercapacitors produced by activation of graphene. Science 2011;332(6037):1537–41.
[16] Baughman RH, Zakhidov AA, Heer WAD. Carbon nanotubes-the route toward applications. Science 2002;297(5582):787–92.
[17] Izadi-Najafabadi A, Yamada T, Futaba DN, Yudasaka M, Takagi H, Hatori H, et al. High-power supercapacitor electrodes from single-walled carbon nanohorn/nanotube composite. ACS Nano 2011;5(2):811–9.
[18] Hahm MG, Reddy ALM, Cole DP, Rivera M, Vento JA, Nam J, et al. Carbon nanotube–nanocup hybrid structures for high power supercapacitor applications. Nano Lett 2012;12(11):1616–5621.
[19] Futaba DN, Hata K, Yamada T, Hiraoka T, Hayamizu Y, Kakudate Y, et al. Shape-engineerable and highly densely packed single-walled carbon nanotubes and their application as super-capacitor electrodes. Nat Mater 2006;5(12):987–94.
[20] Chen C-H, Huang C-C. Hydrogen adsorption in defective carbon nanotubes. Sep Purif Technol 2009;65(3):305–10.
[21] Ko JM, Kim KM. Electrochemical properties of MnO_2/activated carbon nanotube composite as an electrode material for supercapacitor. Mater Chem Phys 2009;114(2–3):837–41.
[22] Lim SH, Elim HI, Gao XY, Wee TS, Ji W, Lee JY, et al. Electronic and optical properties of nitrogen-doped multiwalled carbon nanotubes. Phys Rev B 2006;73(4):045402.
[23] Czerw R, Terrones M, Charlier J-C, Blase X, Foley B, Kamalakaran R, et al. Identification of electron donor states in N-doped carbon nanotubes. Nano Lett 2001;1(9):457–60.
[24] Paek E, Park AJ, Kweon KE, Hwang GS. On the origin of the enhanced supercapacitor performance of nitrogen-doped graphene. J Phys Chem C 2013;117(11):5610–6.
[25] Zhang LL, Zhao X, Ji H, Stoller MD, Lai L, Murali S, et al. Nitrogen doping of graphene and its effect on quantum capacitance, and a new insight on the enhanced capacitance of N-doped carbon. Energy Environ Sci 2012;5(11):9618–25.
[26] Jeong HM, Lee JW, Shin WH, Choi YJ, Shin HJ, Kang JK, et al. Nitrogen-doped graphene for high-performance ultracapacitors and the importance of nitrogen-doped sites at basal planes. Nano Lett 2011;11(6):2472–7.
[27] Perdew JP, Burke K, Ernzerhof M. Generalized gradient approximation made simple. Phys Rev Lett 1996;77(18):3865–8.
[28] Kresse G, Furthmüller J. Efficiency of ab-initio energy calculations for metals and semiconductors using a plane-wave basis set. Comput Mater Sci 1996;6(1):15–50.
[29] Raymundo-Piñero E, Azaïs P, Cacciaguerra T, Cazorla-Amorós D, Linares-Solano A, Béguin F. KOH and NaOH activation mechanisms of multiwalled carbon nanotubes with different structural organization. Carbon 2005;43(4):786–95.
[30] Romanos J, Beckner M, Rash T, Firlej L, Kuchta B, Yu P, et al. Nanospace engineering of KOH activated carbon. Nanotechnology 2012;23(1):015401.
[31] Lee HS, Yun CH, Kim HM, Lee CJ. Persistence length of multiwalled carbon nanotubes with static bending. J Phys Chem C 2007;111(51):18882–7.
[32] Groenewolt M, Antonietti M. Synthesis of g-C_3N_4 nanoparticles in mesoporous silica host matrices. Adv Mater 2005;17(14):1789–92.
[33] Hennrich F, Krupke R, Lebedkin S, Arnold K, Fischer R, Resasco DE, et al. Raman spectroscopy of individual single-walled carbon nanotubes from various sources. J Phys Chem B 2005;109(21):10567–73.
[34] Chipara DM, Macossay J, Ybarra AVR, Chipara AC, Eubanks YM, Chipara M. Raman spectroscopy of polystyrene

nanofibers-multiwalled carbon nanotubes composites. Appl Surf Sci 2013;275(1):23–7.
[35] Telg H, Fouquet M, Maultzsch J, Wu Y, Chandra B, Hone J, et al. G^- and G^+ in the Raman spectrum of isolated nanotube: a study on resonance conditions and lineshape. Phys Status Solidi 2008;245(10):2189–92.
[36] Wang Q, Wen Z, Li J. A hybrid supercapacitor fabricated with a carbon nanotube cathode and a TiO_2-B nanowire anode. Adv Funct Mater 2006;16(16):2141–6.
[37] Chen Z, Augustyn V, Wen J, Zhang Y, Shen M, Dunn B, et al. High-performance supercapacitors based on intertwined CNT/V_2O_5 nanowire nanocomposite. Adv Mater 2011;23(6):791–5.
[38] Kaempgen M, Chan CK, Ma J, Cui Y, Gruner G. Printable thin film supercapacitors using single-walled carbon nanotubes. Nano Lett 2009;9(5):1872–6.